Research Article Vol. 5, No. 1 / January 2018 / Optica 80

Talbot-enhanced, maximum-visibility imaging of condensate interference

Y. Zhai, C. H. Carson, V. A. Henderson, P. F. Griffin, E. Riis, and A. S. Arnold*

Department of Physics, SUPA, University of Strathclyde, Glasgow G4 0NG, UK
**Corresponding author: aidan.arnold@strath.ac.uk*

Received 26 July 2017; revised 5 December 2017; accepted 12 December 2017 (Doc. ID 300731); published 19 January 2018

Nearly two centuries ago Talbot first observed the fascinating effect whereby light propagating through a periodic structure generates a "carpet" of image revivals in the near field. Here we report the first observation of the spatial Talbot effect for light interacting with periodic Bose–Einstein condensate interference fringes. The Talbot effect can lead to dramatic loss of fringe visibility in images, degrading precision interferometry; however, we demonstrate how the effect can also be used as a tool to enhance visibility, as well as extend the useful focal range of matter-wave detection systems by orders of magnitude. We show that negative optical densities arise from matter-wave induced lensing of detuned imaging light—yielding Talbot-enhanced single-shot interference visibility of >135% compared to the ideal visibility for resonant light.

OCIS codes: (020.1475) Bose-Einstein condensates; (020.1335) Atom optics; (110.6760) Talbot and self-imaging effects.
https://doi.org/10.1364/OPTICA.5.000080

1. INTRODUCTION

Since the first experimental realization of gaseous Bose–Einstein condensates (BECs) [1,2], the field has grown dramatically, and condensates are now used for a variety of studies including the flow of superfluids [3], studies of strongly dipolar systems [4,5], and for producing atom lasers [6]. Matter waves are also ideal for quantum technologies, a key ingredient of which is atom interferometry. Interferometers yield precise measurements of fundamental constants [7], rotation [8,9], acceleration [10], gravity [11,12], and gravitational shifts [13]. Interferometry is also a key method for studying the superfluid states prevalent in quantum degenerate systems [14–19].

BECs are fully coherent matter-wave sources, as first strikingly demonstrated in Ref. [20]. A cigar-shaped single-well potential was transformed into a double-well by axial separation with an optical dipole beam. Ballistic expansion led to wavepacket spatial interference, reminiscent of Young's double slits. We use a similar configuration [21], but a simpler levitation-enhanced imaging technique, achieving improved visibility of 80% (Fig. 1) above our previous record of 60% by longer levitation and a weaker dipole beam. BEC interference has also been demonstrated via radial [22–26] or axial [27,28] separation using a wide variety of other techniques. During our BEC interference investigations we observed that the fringe visibility strongly depended on the camera focal location, which we can now clearly attribute to the Talbot effect. Talbot's 1836 observation [29] of self-imaging of a periodic structure in near-field diffraction arises due to wave optics [30]. The phenomenon has since been studied in a wide variety of scientific disciplines including optics, acoustics, electron microscopy, x rays, and plasmonics [31,32]. Transversely coherent waves with wavelength λ passing through a regular phase/intensity structure with period λ_f produce a self-image with a phase of π (0) at odd (even) integer multiples of the Talbot distance $\Lambda_T = \lambda_f^2/\lambda$ [33]. Fractional and fractal Talbot effects arise if the grating structure contains higher spatial harmonics [34].

With matter waves the spatial Talbot effect has been observed from hot atomic beams [35,36], and the temporal Talbot effect has been seen with BECs in 1D optical lattices [37,38]. The effect is also an important trigger for spontaneous spatial light/matter pattern formation in cold atomic gases [39]. Although the regular period and phase of BEC interference patterns are extremely important for metrology, the dramatic influence of the Talbot effect on the propagation of near-resonant light used for imaging condensates has not been previously seen.

Here we present, to the best of our knowledge, the first observation of spatially periodic visibility variation in a BEC interferometer due to the Talbot effect. Imaging light is absorbed and refracted by N BEC interference fringes, and then propagates through the imaging system. At integer Talbot distances $i\Lambda_T$ ($|i| \lesssim N$) from the central image plane the diffracted light dramatically re-images to $N - |i|$ fringes (Fig. 2). Furthermore, by detuning the imaging light, negative optical densities [40] arise, leading to enhanced visibility, nearly doubling the resonant value.

Our results will be of particular relevance to atom interferometry experiments with several fringes ($N > 5$), as opposed to those with only a few fringes or an overall population amplitude

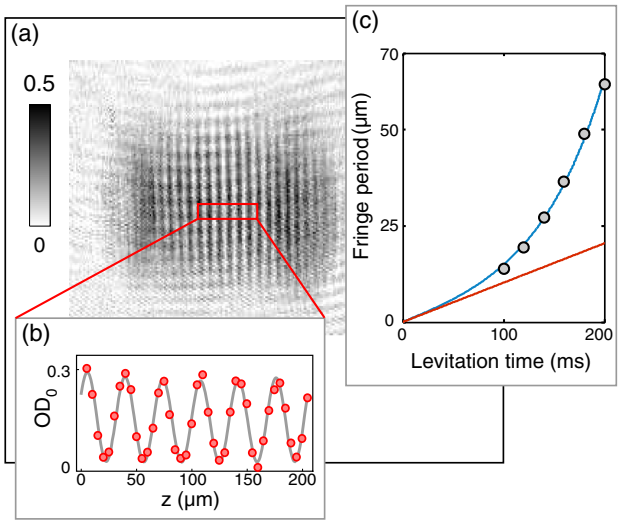

Fig. 1. Matter-wave interference. (a) Experimental absorption image (1.4 mm × 1.4 mm) of a condensate axially split by a blue-detuned optical dipole beam at 160 ms levitation time; scalebar indicates optical density (OD). (b) Background-subtracted, angle-corrected, row-averaged OD profile (red points) of the red rectangular region in (a). The fitted sine wave has a parabolic spatial envelope and offset (gray curve) for fringe visibility and period extraction. (c) Fringe period as a function of levitation time: experimental data (black dots); inferred fringe period evolution [blue curve, Eq. (2) with $\omega_z = 13.8 \pm 1.4$ rad/s and $d = 45$ μm]; ballistic expansion theory [red line, Eq. (1)].

variation. Multi-fringe interferometers may have been optimized in the past based on high visibility, finding only a local maximum. In situations where the fringe period is critical, an assumption of only one image plane could lead to erroneous results [cf. Fig. 2(e)]. In the limit of short period fringes, with period around one wavelength, a Talbot distance of order 1 μm would lead to extreme difficulty in positioning the camera focal plane, with corresponding sensitivity to drift. This would be particularly important if, e.g., single-atom absorption imaging [41] were used in a quantum gas microscope [42,43].

2. EXPERIMENTAL SETUP AND FRINGES

In our experimental setup [21,44], a few 10^8 ^{87}Rb atoms in the weak-field-seeking state $|F = 2, m_F = 2\rangle$ are trapped at the top of a magnetic storage ring [44]. The Ioffe–Pritchard (IP) trap has axial and radial trapping frequencies of 10 and 90 Hz, respectively, and a lifetime of 55 s. After 30 s RF evaporation, condensates with 5×10^5 atoms are created and observed using standard resonant absorption imaging on the stretched D_2 transition $|F = 2, m_F = 2\rangle \rightarrow |F' = 3, m_F = 3\rangle$, with magnification ×2. A 658 nm blue-detuned repulsive dipole beam is used for axial BEC splitting with <1 mW derived from a diode laser with an acousto-optic modulator focused to a 10 μm waist [21].

Split BECs are released by rapidly switching off the optical and magnetic potential, and they expand in space for sufficiently long that the final atomic cloud size is much larger than the initial distribution. Thus even initial spatial distributions with some broken symmetry behave like two matter-wave point sources. This leads to clear "Young's-slit" type planar interference patterns

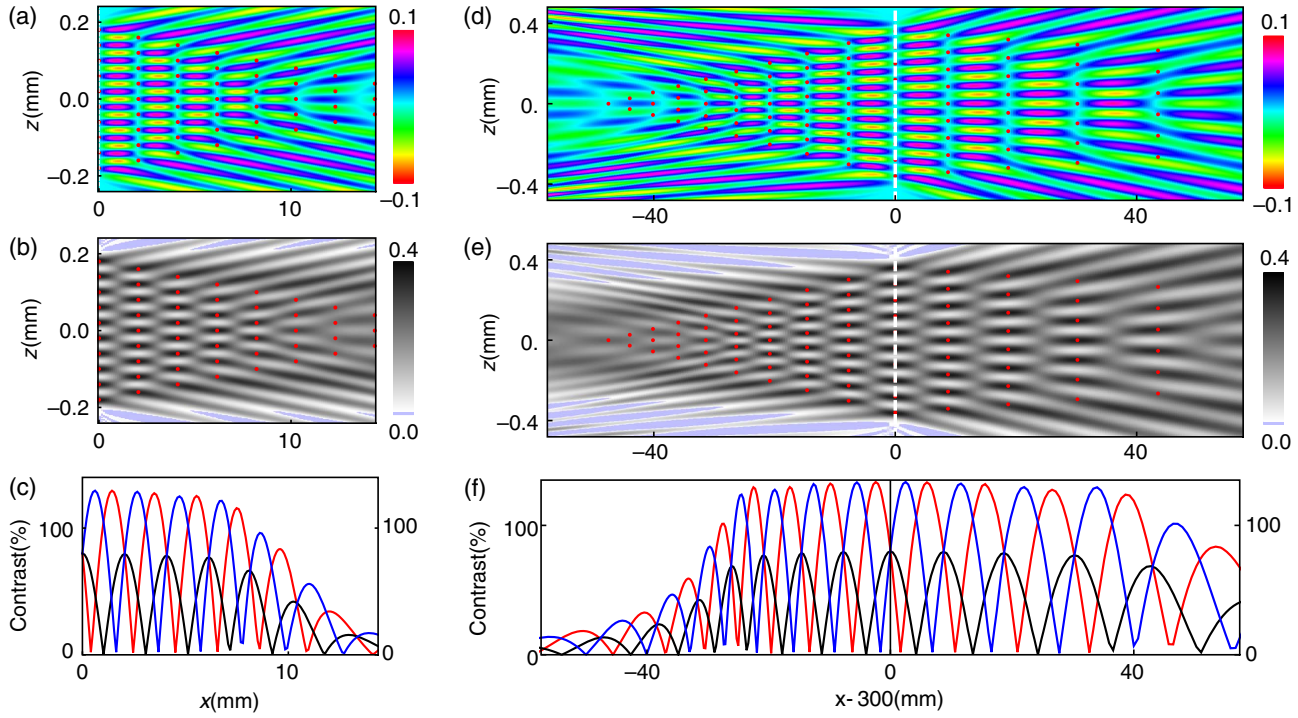

Fig. 2. Theoretical light propagation through BEC fringes. (a)–(c) Ten BEC fringes along $x = 0$ of peak optical density $OD_0 = 0.4$ and visibility 80% interact with resonant light leading, on propagation ($x > 0$), to periodic phase [(a) in radians] and OD (b) profile revivals. Antinodes of OD (red points) correspond to nodes of the phase, and vice versa. The central fringe at $z = 0$ is displayed (c) for red, resonant (black), and blue laser detunings of $-\Gamma/2$, 0, and $\Gamma/2$, illustrating how detuning not only phase-shifts the fringes in x, but can also enhance visibility relative to the initial optical density. After the light in images (a), (b), and (c) propagates through a 300-mm-long ×2 magnification imaging system, the corresponding phase, OD, and visibility are shown in (d), (e), and (f), respectively. Note the chirp in the spatial period about the image plane [white dashed line in (d) and (e)].

in 3D [Figs. 1(a) and 1(b)], obviating the need for specialized tomographic imaging [20]. The BEC fringe period λ_f comes from the de Broglie wavelength of the two condensates and can be expressed as

$$\lambda_f = \frac{ht}{md}, \tag{1}$$

where h is Planck's constant, t the ballistic expansion time, m is the atomic mass, and d is the initial BEC center-of-mass separation. The freefall time is limited to 0–30 ms by the size of the imaging area, and times <60 ms by the physical extent of the vacuum cell. To overcome these limitations we use a magnetic levitation field [1,45,46] derived from a toroidal quadrupole [44] offset by an additional vertical constant field. BECs therefore experience a weak inverted parabola potential ($U_z = -m\omega_z^2 z^2/2$ with ω_z the angular velocity along the z direction, i.e., the BEC axis) due to the circular nature of the levitation coils, which we showed in Ref. [21] modifies λ_f in Eq. (1) to

$$\lambda_f' = \lambda_f \frac{\sinh(\omega_z t)}{\omega_z t}. \tag{2}$$

Although our initial BEC separation d is large in comparison to other experiments, the levitation potential we apply magnifies the spatial scale of our fringes [17,21] [Fig. 1(c)]. To achieve the equivalent maximum fringe period by ballistic expansion we would need 800 ms, i.e., 3 m of freefall. To resolve the fringes levitation times ≥70 ms are needed until the period corresponds to two or more camera pixels (≥10 μm). Using resonant light absorption imaging fringe periods of 37.5(0.8) μm are observed, with the highest visibility seen in this type of interferometer—80% [Figs. 1(a) and 1(b)]—close to the theoretical limit due to camera pixelation of the fringes. Depending on the timing and power of the dipole beam application either two phase-separate condensates are created or a single condensate can be split into two phase-coherently [22,47]. The size of our interference pattern in comparison to our center-of-mass uncertainty currently prevents us from ascertaining whether the relative phases of our split condensates are random or correlated; however, the main results are unaffected.

3. TALBOT EFFECT: THEORY AND EXPERIMENT

The effect of imaging light interacting with periodic BEC fringes can be modeled by Fourier-propagating the light waves, based on the initial conditions of the field immediately after the condensate, and then performing the inverse Fourier transform to convert back to real space [48–51]. Propagation effects inside the BEC are neglected as the condensate size in the beam propagation direction is considerably smaller than the Talbot period.

When light passes through the BEC fringes, the light attenuation and phase shift depend on the light detuning and the integrated atomic density. In the standard absorption imaging we use, the light passing through the atomic cloud indicates a transversely spatially dependent optical density

$$\mathrm{OD} = \ln\left(\frac{I_i - I_b}{I_e - I_b}\right), \tag{3}$$

where I_i, I_e, and I_b are the light intensity distributions incident on the atoms, exiting the atoms, and due to background light, respectively. For low-intensity light the optical density in the BEC pattern varies with detuning as $\mathrm{OD} = \mathrm{OD}_0/(1 + 4(\Delta/\Gamma)^2)$, where Δ is the light detuning from the atomic resonance, OD_0 is the (resonant) peak optical density, and Γ is the natural linewidth. In our system Γ is power-broadened from 6 to 8 MHz. The light phase shift due to the BEC is given via the Kramers–Kronig relation, i.e., $\delta\phi = -\mathrm{OD}\Delta/\Gamma$, with a maximum phase shift at $\Delta = \pm\Gamma/2$. Under conditions similar to Fig. 1(b), with $\mathrm{OD}_0 = 0.4$ and $\Delta = 0$ MHz, in Fig. 2 we investigate the theoretical fringe behavior for 10 BEC fringes with $\mathrm{OD}_0 = 0.4$ and visibility 80% observed with on-resonant imaging, as well as the key effect of changing the imaging beam detuning (Fig. 2).

By taking z slices through the Talbot optical density "carpet" in Figs. 2(b) and 2(e), the visibility as a function of x for imaging detuning $\Delta = 0$ MHz can be obtained, and compared to the behavior for detunings $\Delta = \pm 4$ MHz [Figs. 2(c) and 2(f)]. The model we use to fit fringes at a given z is a sine wave of visibility C, modulated by a parabolic amplitude to incorporate the typical experimental behavior of the fringes due to their origin from the overlap of two initially spatially separated clouds:

$$(A_0 + A_2(z - z_0)^2)(C\,\sin(kz + \phi) + 1). \tag{4}$$

Visibilities $C > 1$ occur when the absorption imaging beam shows regions of negative optical density—where more light is in the beam after it passes through the BEC fringes than before—a single-shot experimental example of which is shown in Fig. 3(a) with $C \approx 150\%$. Figure 3(b) presents the corresponding spatial Talbot experimental visibility data to Fig. 2(e), at the same detunings, for imaging light interacting with periodic BEC fringes. For both positive and negative detuned light the experimental and theoretical visibility agree well and are enhanced from 80% to 135% [Fig. 3(b)]. This visibility enhancement for detuned light is due to the phase variation in the initial conditions converting reversibly into intensity variation upon propagation. The enhancement can also be interpreted as focusing since the sinusoidal spatial phase variation is like a collection of alternating positive and negative lenses.

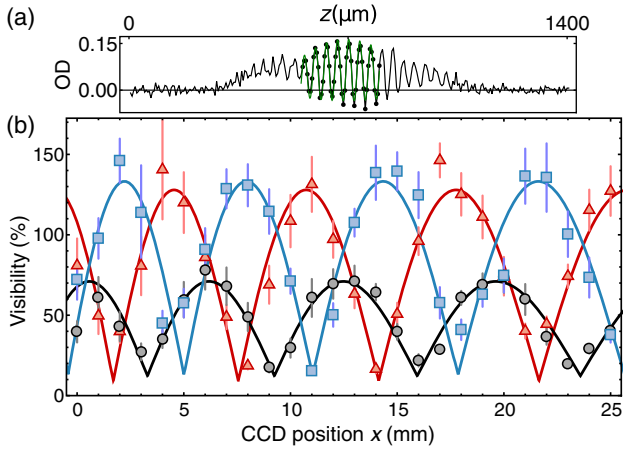

Fig. 3. (a) Single-shot 1D BEC OD profile (21 row average, $\Delta = +4$ MHz), with visibility $C = 1.5$ from fitting data points (black) with Eq. (4) (green curve). (b) Experimental (dots) and theoretical [curves from Fig. 2(e)] visibility as a function of camera position for detunings −4, 0, and +4 MHz (red, black, and blue, respectively). All error bars in this paper represent the standard deviation of results from three separate images. The central Talbot period was fit to be 6.1(0.1) mm, which agrees well with the theoretical Talbot period of 6.4(0.3) mm predicted from the fringe period and Eq. (5).

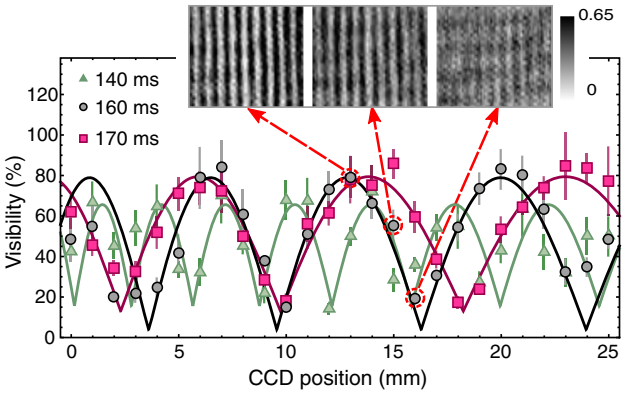

Fig. 4. Talbot period variation with fringe period. Visibility is observed as a function of camera position for $\Delta = +0.5$ MHz imaging light after 140, 160, and 170 ms levitation. From fits to these data Talbot periods were measured to be 3.0(0.1) mm, 6.1(0.2) mm, and 7.6(0.2) mm, respectively, which agree with the theoretical Talbot periods of 3.4(0.1) mm, 6.3(0.2) mm, and 8.1(0.8) mm determined from the experimental fringe periods associated with the 140, 160, and 170 ms levitation times. Inset optical density plots (320 μm × 280 μm) show the observed visibility changing through the Talbot period.

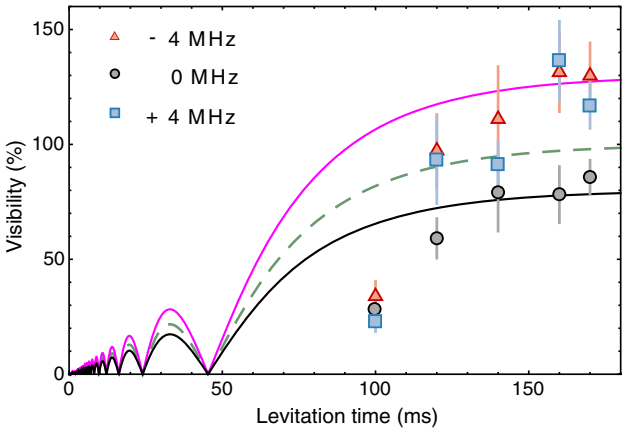

Fig. 5. Interference visibility as a function of levitation time and imaging detuning. Red triangles, black circles and blue squares denote detunings $\Delta = -4$ MHz, 0 MHz, and +4 MHz, respectively. For comparison theory curves are provided of optimal visibility using Eq. (6) with pixelation-free final visibility values of $C = 0.8$, 1.0, and 1.3, shown by the black, green, and cyan curves, respectively. The C values 0.8 and 1.3 are chosen to approximately match the theoretical and experimental values from Figs. 2 and 3, where $OD_0 = 0.4$.

The variation of the observed fringe visibility as a function of the camera position can be attributed to the Talbot effect. The magnification of the imaging system modifies the Talbot period, which is therefore given by

$$\Lambda = \frac{(M\lambda_f)^2}{\lambda}, \tag{5}$$

for light of wavelength λ incident on a periodic density/phase modulation of period λ_f, where M is the camera magnification. With the camera position at 13 mm, the observed fringe period on the CCD for on-resonance light in Fig. 3 was 70.9(1.5) μm. The corresponding Talbot period was measured to be 6.1(0.1) mm, which is in good agreement with the theoretically predicted Talbot period of 6.4(0.3) mm.

To verify that the Talbot effect was at work, we changed the period of the interference pattern, thus changing the Talbot period. The fringe period was altered by using different levitation times [Fig. 1(c)]; 140 and 170 ms were chosen as they would result in a notable change in the observed Talbot period. The fringe period under the experimental conditions in Fig. 4, with the camera at 13 mm and $\Delta = +0.5$ MHz, were measured to be 51.2(0.3) μm and 79.5(3.7) μm for 140 and 170 ms, respectively. The measured Talbot periods were found to be 3.0(0.1) mm for 140 ms and 7.6(0.2) mm for 170 ms, which are also in good agreement with the theoretical Talbot periods of 3.4(0.1) mm and 8.1(0.8) mm for 140 and 170 ms, respectively. Figure 4 also presents density plots of the interference fringes at the peak, middle, and trough of a Talbot period, showing the drastic change the spatial Talbot effect can have on the interference signal.

4. OPTIMAL VISIBILITY

In Fig. 5 fringe visibility versus expansion time is shown for both experiment and theory, with experimental data reaching the highest visibility reported in this type of interferometer. Note that for each detuning in Fig. 5 the data at different levitation times were selected from the peak value within one Talbot period. For comparison to our experimental visibility versus levitation time results shown in Fig. 5, we first consider the theoretical maximum visibility that can be reached. Assuming two perfect matter-wave point sources, sinusoidal interference fringes result of the form $F(x) = 1 + C\ \sin(2\pi x/\lambda_f)$, where λ_f is the fringe period, and C is the visibility. When these fringes hit the jth pixel of a perfect CCD camera, with pixel size l, the fringe signal averaged over the range $(j - 1/2)l \le x \le (j + 1/2)l$ is

$$F_{\mathrm{CCD}} = 1 + \mathrm{sinc}(\pi l/\lambda_f) C\ \sin(2\pi j l/\lambda_f); \tag{6}$$

i.e., the original fringe visibility C reduces to $C' = \mathrm{sinc}(\pi l/\lambda_f)C$. In our experiment $l = 5$ μm is constant, and the visibility only depends on the time-dependent fringe period—which we know from the fit to Eq. (2) in Fig. 1(c). This allows us to determine the theoretical maximum-visibility sinc curves shown in Fig. 5, which for levitation times after 120 ms reach visibilities more than $0.95C$ and are surprisingly similar to experimental data. This is quite remarkable as in the theory we assumed perfect matter-wave point sources without any allowance for our non-tomographic imaging, which is susceptible to any spatial asymmetry in the source BECs and hence 3D curvature of the fringes (cf. Ref. [20]). The reason for a resonant contrast <100% is attributed to either a slight angle between the fringe planes and the imaging beam **k**-vector or population asymmetry in the split BECs; however, it is still the highest resonant visibility seen in this type of interferometer.

5. CONCLUSIONS

We report, to the best of our knowledge, the first observation of the spatial Talbot effect of imaging light interacting with periodic BEC interference fringes. This interpretation is confirmed by the strong agreement between the Talbot lengths predicted by the fringe period and the measured Talbot periods from the experimental data. We have shown that the spatial Talbot effect can

have drastic effects on the interference signal, and is therefore relevant for all BEC interferometers. More importantly, this effect can then be used as a tool, or diagnostic, to focus interference experiment imaging systems and help obtain the maximum possible visibility. By using detuned imaging light (±4 MHz) the Talbot effect converts the imaging light periodic phase shift from the BEC fringes into an intensity ripple, which results in an increase in the observed fringe visibility. This enhancement in visibility allows us to observe single-shot interference visibility [as defined in Eq. (4)] of $C > 135\%$, which is the highest ever reported in this type of interferometer. Such a contrast is not unphysical because the Talbot effect redistributes light into different parts of the absorption imaging beam—leading to some beam regions with increased power, i.e., negative optical densities. The limit to attaining even higher visibility is probably due to the underlying 80% resonant visibility. This is due to either a slight angle between the imaging beam and the fringes or population imbalance in the split BEC—we have shown that it is unlikely to be due to CCD camera pixelation.

Talbot-enhanced interferometers will be particularly advantageous in situations where the fringe period/camera pixel size ratio is small (or even less than 1), as the longer Talbot period can be used to accurately infer the matter-wave fringe period. Moreover, by appropriately tailoring the incident imaging light to have variable focal distance (e.g., with a variable focus lens [52]), the entire 2D Talbot carpet [Fig. 2(e)] can be mapped out automatically. With the modification of varying imaging light propagation direction (e.g., with crossed AOMs [53–55]) and a single-pixel detector [56], this would extend the scheme to short imaging wavelength detection and enable *single-shot* 2D Talbot mapping. Access to the full 2D Talbot carpet would enable more accurate phase determination of the fringes.

An advantage of our axial inverted parabolic levitation potential is that even in a compact vacuum system, with large initial condensate separation, it exponentially magnifies fringe periods to the same level seen in drop-tower [12] and 10 m vacuum experiments [57]; however, a caveat is that samples in the potential are also exponentially sensitive to initial position and velocity. In the future we will enable accurate metrology with the interferometer by reducing our rms center-of-mass noise. To further increase future interferometer phase accumulation time, the split BEC matter waves could be guided in a waveguide [58] or ring trap [44,59–62], and delta kicking could be used to minimize the atomic velocity spread [57,63,64].

The dataset for this paper is available online Dataset 1, Ref. [65].

Funding. Leverhulme Trust (RPG-2013-074); Defence Science and Technology Laboratory (DSTL) (DSTLX-1000095638R); Engineering and Physical Sciences Research Council (EPSRC) (EP/M013294/1).

Acknowledgment. We greatly appreciate valuable discussions with T. Ackemann, G.-L. Oppo, G. R. M. Robb, and W. J. Firth.

REFERENCES

1. M. H. Anderson, J. R. Ensher, M. R. Matthews, C. E. Wieman, and E. A. Cornell, "Observation of Bose-Einstein condensation in a dilute atomic vapor," Science **269**, 198–201 (1995).
2. K. B. Davis, M.-O. Mewes, M. R. Andrews, N. J. van Druten, D. S. Durfee, D. M. Kurn, and W. Ketterle, "Bose-Einstein condensation in a gas of sodium atoms," Phys. Rev. Lett. **75**, 3969–3973 (1995).
3. C. Ryu, M. F. Andersen, P. Cladé, V. Natarajan, K. Helmerson, and W. D. Phillips, "Observation of persistent flow of a Bose-Einstein condensate in a toroidal trap," Phys. Rev. Lett. **99**, 260401 (2007).
4. M. Lu, N. Q. Burdick, S. H. Youn, and B. L. Lev, "Strongly dipolar Bose-Einstein condensate of dysprosium," Phys. Rev. Lett. **107**, 190401 (2011).
5. K. Aikawa, A. Frisch, M. Mark, S. Baier, A. Rietzler, R. Grimm, and F. Ferlaino, "Bose-Einstein condensation of erbium," Phys. Rev. Lett. **108**, 210401 (2012).
6. N. P. Robins, C. Figl, S. A. Haine, A. K. Morrison, M. Jeppesen, J. J. Hope, and J. D. Close, "Achieving peak brightness in an atom laser," Phys. Rev. Lett. **96**, 140403 (2006).
7. S. Gupta, K. Dieckmann, Z. Hadzibabic, and D. E. Pritchard, "Contrast interferometry using Bose-Einstein condensates to measure h/m and α," Phys. Rev. Lett. **89**, 140401 (2002).
8. T. L. Gustavson, A. Landragin, and M. A. Kasevich, "Rotation sensing with a dual atom-interferometer Sagnac gyroscope," Classical Quantum Gravity **17**, 2385–2398 (2000).
9. T. L. Gustavson, P. Bouyer, and M. A. Kasevich, "Precision rotation measurements with an atom interferometer gyroscope," Phys. Rev. Lett. **78**, 2046–2049 (1997).
10. J. M. McGuirk, M. J. Snadden, and M. A. Kasevich, "Large area light-pulse atom interferometry," Phys. Rev. Lett. **85**, 4498–4501 (2000).
11. A. Peters, K. Y. Chung, and S. Chu, "High-precision gravity measurements using atom interferometry," Metrologia **38**, 25–61 (2001).
12. H. Müntinga, H. Ahlers, M. Krutzik, A. Wenzlawski, S. Arnold, D. Becker, K. Bongs, H. Dittus, H. Duncker, N. Gaaloul, C. Gherasim, E. Giese, C. Grzeschik, T. W. Hänsch, O. Hellmig, W. Herr, S. Herrmann, E. Kajari, S. Kleinert, C. Lämmerzahl, W. Lewoczko-Adamczyk, J. Malcolm, N. Meyer, R. Nolte, A. Peters, M. Popp, J. Reichel, A. Roura, J. Rudolph, M. Schiemangk, M. Schneider, S. T. Seidel, K. Sengstock, V. Tamma, T. Valenzuela, A. Vogel, R. Walser, T. Wendrich, P. Windpassinger, W. Zeller, T. van Zoest, W. Ertmer, W. P. Schleich, and E. M. Rasel, "Interferometry with Bose-Einstein condensates in microgravity," Phys. Rev. Lett. **110**, 093602 (2013).
13. H. Müller, A. Peters, and S. Chu, "A precision measurement of the gravitational redshift by the interference of matter waves," Nature **463**, 926–929 (2010).
14. S. Inouye, S. Gupta, T. Rosenband, A. P. Chikkatur, A. Görlitz, T. L. Gustavson, A. E. Leanhardt, D. E. Pritchard, and W. Ketterle, "Observation of vortex phase singularities in Bose-Einstein condensates," Phys. Rev. Lett. **87**, 080402 (2001).
15. Z. Hadzibabic, P. Krüger, M. Cheneau, B. Battelier, and J. Dalibard, "Berezinskii-Kosterlitz-Thouless crossover in a trapped atomic gas," Nature **441**, 1118–1121 (2006).
16. S. Hofferberth, I. Lesanovsky, B. Fischer, T. Schumm, and J. Schmiedmayer, "Non-equilibrium coherence dynamics in one-dimensional Bose gases," Nature **449**, 324–327 (2007).
17. C. Kohstall, S. Riedl, E. R. Sánchez Guajardo, L. A. Sidorenkov, J. Hecker Denschlag, and R. Grimm, "Observation of interference between two molecular Bose-Einstein condensates," New J. Phys. **13**, 065027 (2011).
18. S. Eckel, F. Jendrzejewski, A. Kumar, C. J. Lobb, and G. K. Campbell, "Interferometric measurement of the current-phase relationship of a superfluid weak link," Phys. Rev. X **4**, 031052 (2014).
19. L. Corman, L. Chomaz, T. Bienaimé, R. Desbuquois, C. Weitenberg, S. Nascimbène, J. Dalibard, and J. Beugnon, "Quench-induced supercurrents in an annular Bose gas," Phys. Rev. Lett. **113**, 135302 (2014).
20. M. R. Andrews, C. G. Townsend, H.-J. Miesner, D. S. Durfee, D. M. Kurn, and W. Ketterle, "Observation of interference between two Bose condensates," Science **275**, 637–641 (1997).
21. M. E. Zawadzki, P. F. Griffin, E. Riis, and A. S. Arnold, "Spatial interference from well-separated split condensates," Phys. Rev. A **81**, 043608 (2010).
22. Y. Shin, M. Saba, T. A. Pasquini, W. Ketterle, D. E. Pritchard, and A. E. Leanhardt, "Atom interferometry with Bose-Einstein condensates in a double-well potential," Phys. Rev. Lett. **92**, 050405 (2004).
23. C. Ryu and M. G. Boshier, "Integrated coherent matter wave circuits," New J. Phys. **17**, 092002 (2015).

24. Y. Shin, C. Sanner, G.-B. Jo, T. A. Pasquini, M. Saba, W. Ketterle, D. E. Pritchard, M. Vengalattore, and M. Prentiss, "Interference of Bose-Einstein condensates split with an atom chip," Phys. Rev. A **72**, 021604(R) (2005).
25. T. Schumm, S. Hofferberth, L. M. Andersson, S. Wildermuth, S. Groth, I. Bar-Joseph, J. Schmiedmayer, and P. Krüger, "Matter-wave interferometry in a double well on an atom chip," Nat. Phys. **1**, 57–62 (2005).
26. S. Machluf, Y. Japha, and R. Folman, "Coherent Stern-Gerlach momentum splitting on an atom chip," Nat. Commun. **4**, 2424 (2013).
27. O. Garcia, B. Deissler, K. J. Hughes, J. M. Reeves, and C. A. Sackett, "Bose-Einstein-condensate interferometer with macroscopic arm separation," Phys. Rev. A **74**, 031601 (2006).
28. Y.-J. Wang, D. Z. Anderson, V. M. Bright, E. A. Cornell, Q. Diot, T. Kishimoto, M. Prentiss, R. A. Saravanan, S. R. Segal, and S. Wu, "Atom Michelson interferometer on a chip using a Bose-Einstein condensate," Phys. Rev. Lett. **94**, 090405 (2005).
29. H. F. Talbot, "Facts relating to optical science," Philos. Mag. **9**(56), 401–407 (1836).
30. Lord Rayleigh, "On copying diffraction-gratings, and on some phenomena connected therewith," Philos. Mag. **11**, 196–205 (1881).
31. K. Patorski, "The self-imaging phenomenon and its applications," Prog. Opt. **27**, 1–108 (1989).
32. J. Wen, Y. Zhang, and M. Xiao, "The Talbot effect: recent advances in classical optics, nonlinear optics, and quantum optics," Adv. Opt. Photon. **5**, 83–130 (2013).
33. A. D. Cronin, J. Schmiedmayer, and D. E. Pritchard, "Optics and interferometry with atoms and molecules," Rev. Mod. Phys. **81**, 1051–1129 (2009).
34. M. V. Berry and S. Klein, "Integer, fractional and fractal Talbot effects," J. Mod. Opt. **43**, 2139–2164 (1996).
35. M. S. Chapman, C. R. Ekstrom, T. D. Hammond, J. Schmiedmayer, B. E. Tannian, S. Wehinger, and D. E. Pritchard, "Near-field imaging of atom diffraction gratings: the atomic Talbot effect," Phys. Rev. A **51**, R14–R17 (1995).
36. S. Nowak, Ch. Kurtsiefer, T. Pfau, and C. David, "High-order Talbot fringes for atomic matter waves," Opt. Lett. **22**, 1430–1432 (1997).
37. L. Deng, E. W. Hagley, J. Denschlag, J. E. Simsarian, M. Edwards, C. W. Clark, K. Helmerson, S. L. Rolston, and W. D. Phillips, "Temporal, matter-wave-dispersion Talbot effect," Phys. Rev. Lett. **83**, 5407–5411 (1999).
38. M. J. Mark, E. Haller, J. G. Danzl, K. Lauber, M. Gustavsson, and H.-C. Nägerl, "Demonstration of the temporal matter-wave Talbot effect for trapped matter waves," New J. Phys. **13**, 085008 (2011).
39. G. Labeyrie, E. Tesio, P. M. Gomes, G.-L. Oppo, W. J. Firth, G. R. M. Robb, A. S. Arnold, R. Kaiser, and T. Ackemann, "Optomechanical self-structuring in a cold atomic gas," Nat. Photonics **8**, 321–325 (2014).
40. C. Ryu, K. C. Henderson, and M. G. Boshier, "Creation of matter wave Bessel beams and observation of quantized circulation in a Bose–Einstein condensate," New J. Phys. **16**, 013046 (2014).
41. E. W. Streed, A. Jechow, B. G. Norton, and D. Kielpinski, "Absorption imaging of a single atom," Nat. Commun. **3**, 933 (2012).
42. W. S. Bakr, A. Peng, M. E. Tai, R. Ma, J. Simon, J. I. Gillen, S. Fölling, L. Pollet, and M. Greiner, "Probing the superfluid-to-Mott insulator transition at the single-atom level," Science **329**, 547–550 (2010).
43. J. F. Sherson, C. Weitenberg, M. Endres, M. Cheneau, I. Bloch, and S. Kuhr, "Single-atom-resolved fluorescence imaging of an atomic Mott insulator," Nature **467**, 68–72 (2010).
44. A. S. Arnold, C. S. Garvie, and E. Riis, "Large magnetic storage ring for Bose-Einstein condensates," Phys. Rev. A **73**, 041606(R) (2006).
45. T. Weber, M. Herbig, M. Mark, H.-C. Nägerl, and R. Grimm, "Bose-Einstein condensation of cesium," Science **299**, 232–235 (2003).
46. D. J. Han, M. T. DePue, and D. S. Weiss, "Loading and compressing Cs atoms in a very far-off-resonant light trap," Phys. Rev. A **63**, 023405 (2001).
47. G.-B. Jo, Y. Shin, S. Will, T. A. Pasquini, M. Saba, W. Ketterle, D. E. Pritchard, M. Vengalattore, and M. Prentiss, "Long phase coherence time and number squeezing of two Bose-Einstein condensates on an atom chip," Phys. Rev. Lett. **98**, 030407 (2007).
48. A. McDonald, G. McConnell, D. C. Cox, E. Riis, and P. F. Griffin, "3D mapping of intensity field about the focus of a micrometer-scale parabolic mirror," Opt. Express **23**, 2375–2382 (2015).
49. V. A. Henderson, P. F. Griffin, E. Riis, and A. S. Arnold, "Comparative simulations of Fresnel holography methods for atomic waveguides," New J. Phys. **18**, 025007 (2016).
50. L. Novotny and B. Hecht, *Principles of Nano-Optics* (Cambridge University, 2012).
51. J. Goodman, *Introduction to Fourier Optics* (Roberts, 2005).
52. J. Léonard, M. Lee, A. Morales, T. M. Karg, T. Esslinger, and T. Donner, "Optical transport and manipulation of an ultracold atomic cloud using focus-tunable lenses," New J. Phys. **16**, 093028 (2014).
53. M. O. Mewes, M. R. Andrews, N. J. van Druten, D. M. Kurn, D. S. Durfee, C. G. Townsend, and W. Ketterle, "Collective excitations of a Bose-Einstein condensate in a magnetic trap," Phys. Rev. Lett. **77**, 988–991 (1996).
54. N. Houston, E. Riis, and A. S. Arnold, "Reproducible dynamic dark ring lattices for ultracold atoms," J. Phys. B **41**, 211001 (2008).
55. K. Henderson, C. Ryu, C. MacCormick, and M. G. Boshier, "Experimental demonstration of painting arbitrary and dynamic potentials for Bose–Einstein condensates," New J. Phys. **11**, 043030 (2009).
56. B. Sun, M. P. Edgar, R. Bowman, L. E. Vittert, S. Welsh, A. Bowman, and M. J. Padgett, "3D computational imaging with single-pixel detectors," Science **340**, 844–847 (2013).
57. T. Kovachy, J. M. Hogan, A. Sugarbaker, S. M. Dickerson, C. A. Donnelly, C. Overstreet, and M. A. Kasevich, "Matter wave lensing to picokelvin temperatures," Phys. Rev. Lett. **114**, 143004 (2015).
58. K. Bongs, S. Burger, S. Dettmer, D. Hellweg, J. Arlt, W. Ertmer, and K. Sengstock, "Waveguide for Bose-Einstein condensates," Phys. Rev. A **63**, 031602 (2001).
59. S. Gupta, K. W. Murch, K. L. Moore, T. P. Purdy, and D. M. Stamper-Kurn, "Bose-Einstein condensation in a circular waveguide," Phys. Rev. Lett. **95**, 143201 (2005).
60. J. D. Pritchard, A. N. Dinkelaker, A. S. Arnold, P. F. Griffin, and E. Riis, "Demonstration of an inductively coupled ring trap for cold atoms," New J. Phys. **14**, 103047 (2012).
61. G. A. Sinuco-León, K. A. Burrows, A. S. Arnold, and B. M. Garraway, "Inductively guided circuits for ultracold dressed atoms," Nat. Commun. **5**, 5289 (2014).
62. T. A. Bell, J. A. P. Glidden, L. Humbert, M. W. J. Bromley, S. A. Haine, M. J. Davis, T. W. Neely, M. A. Baker, and H. Rubinsztein-Dunlop, "Bose-Einstein condensation in large time-averaged optical ring potentials," New J. Phys. **18**, 035003 (2016).
63. A. S. Arnold, C. MacCormick, and M. G. Boshier, "Adaptive inelastic magnetic mirror for Bose-Einstein condensates," Phys. Rev. A **65**, 031601 (2002).
64. N. K. Efremidis, V. Paltoglou, and W. von Klitzing, "Accelerating and abruptly autofocusing matter waves," Phys. Rev. A **87**, 043637 (2013).
65. A. S. Arnold, V. Henderson, C. H. Carson, Y. Zhai, P. Griffin, and E. Riis, "Data for: "Talbot-enhanced, maximum-visibility imaging of condensate interference"" University of Strathclyde (2017) [retrieved 19 December 2017], https://doi.org/10.15129/41d43433-6ddb-4b6e-8040-51b61df2bb39.